Estimating Vertical Motion Profile Top-Heaviness: Reanalysis Compared to Satellite-Based Observations and Stratiform Rain Fraction

LARISSA E. BACK, ZACHARY HANSEN, AND ZACHARY HANDLOS

Department of Atmospheric and Oceanic Sciences, University of Wisconsin–Madison, Madison, Wisconsin

(Manuscript received 24 February 2016, in final form 6 December 2016)

ABSTRACT

A method for representing geographic variability in vertical motion profile top-heaviness in reanalysis data is introduced. The results from this method are compared to a satellite-based method for estimating top-heaviness of vertical motion profiles over the oceans. The satellite-based method utilizes basis functions, idealized or from reanalysis, along with scatterometer wind convergence data and rainfall to estimate the top-heaviness of the vertical motion profile. Results from the two methods of estimating top-heaviness are significantly correlated. Both estimates of top-heaviness are compared to stratiform, shallow, and convective rain fraction. Findings show geographic variability in stratiform rain fraction is not well correlated with estimated profile top-heaviness. Shallow rain fraction is not variable enough to explain this finding. The results may be due to geographic variations in the shape of convective or stratiform heating profiles. An example is given of how variations in convective heating profiles could lead to a region with more stratiform rain having a more bottom-heavy profile.

1. Background

Tropical large-scale vertical motion profiles are important for a wide variety of dynamics problems. However, they are difficult to measure, simulate, and estimate, and basic science questions about what controls profile shape, or "top heaviness," remain to be determined. The term top-heaviness in this work is used to refer to the extent to which vertical motion peaks in the upper troposphere compared to lower in the troposphere. In this work, we compare climatological vertical motion profile shapes (top heaviness) estimated from the ERA-Interim to satellite-based estimates of top-heaviness, as well as the fraction of rain that falls as stratiform, shallow, and convective rain. We find that stratiform and shallow rain fraction do not explain geographic variability in vertical motion profiles and discuss why this may be the case.

Vertical motion profiles and latent heating profiles are closely intertwined, as can be seen from the dry static energy budget (e.g., Yanai et al. 1973; Handlos and Back 2014). Temperature tendencies on longer-than-diurnal time scales and horizontal advection are small in the tropics owing to the large Rossby radius and gravity waves quickly distributing heating anomalies (Charney 1963; Bretherton and Smolarkiewicz 1989; Sobel and Bretherton 2000). Hence, the dominant balance in the energy budget is between vertical advection of dry static energy and "apparent heating," which consists of heating due to radiation, the release of latent heating by condensation, and vertical convergence of the vertical eddy transport of sensible heat. The latter term is primarily important in the subcloud layer and latent heating is more variable than radiative heating. Hence, we can think of the vertical profile of latent heating as closely tied to vertical profile of vertical motion.

A number of studies have looked at the response of the circulation to variations in latent heating profile shape and shown that these variations have an impact on the large-scale circulation (e.g., Hartmann et al. 1984; Wu et al. 2000; Schumacher et al. 2004) when latent heating profile variations are imposed in numerical models. This suggests that simulating these correctly is critical to simulations of large-scale tropical circulations.

More recently, energetic frameworks for thinking about mean ITCZ shifts have gained popularity (e.g., Kang et al. 2009; Frierson et al. 2013; Schneider et al. 2014). This approach can even be generalized to zonally varying ITCZ shifts (Adam et al. 2016). In these frameworks, quantities related to the gross moist stability are critical to determining the size of the response

Corresponding author e-mail: Larissa E. Back, lback@wisc.edu

DOI: 10.1175/JAS-D-16-0062.1

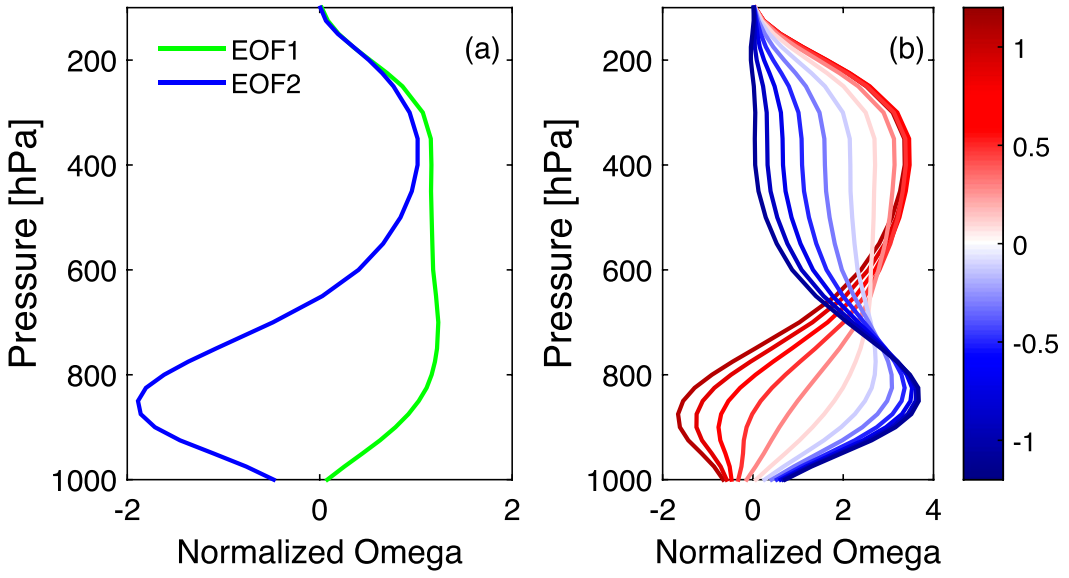

FIG. 1. (a) First two EOFs from a principal component analysis of vertical motion profile variability as a function of height. (b) Vertical motion profile shapes constructed from given top-heaviness ratios of EOF2 to EOF1. Colors correspond to those in Fig. 2.

of the ITCZ to extratropical forcing or how far off the equator the ITCZ is located. The vertical structure of convection has a strong influence on the gross moist stability (e.g., Back and Bretherton 2006), so the vertical motion and latent heating profile of the convection influences where the ITCZ is in these theories. This provides added motivation for documenting and understanding controls on vertical motion profiles.

Other recent work has suggested that the extent to which bottom-heavy circulations are simulated may influence modeled climate sensitivity (Sherwood et al. 2014). This correlation supports analyzing where bottom-heavy circulations exist in nature, using satellite or other data.

In this work, we introduce a principal component analysis–based method for examining the climatological shape of vertical motion profiles in reanalysis in section 2. We also use satellite data to estimate vertical motion profile shape (section 2a). We compare to Tropical Rainfall Measurement Mission (TRMM) climatological estimates of stratiform and shallow rain fraction and look at the relationship between the top-heaviness metrics and these quantities (section 2b). We discuss possible reasons for the lack of relationship we see in section 3. Finally, we summarize our conclusions in section 4.

2. Analysis

We perform a principal component analysis of vertical motion using monthly mean pressure level data from ERA-Interim (Dee et al. 2011) for 2001–06. The analysis is performed by placing each gridpoint month corresponding to ocean regions at a latitude less than 20° into a large space-agnostic matrix. Then, we perform the analysis in such a way that it produces empirical orthogonal functions (EOFs) that have vertical motion as a function of height and principal components that are functions of space and time.

The first two EOFs of vertical motion are shown in Fig. 1a and explain 71.2% and 15.8% of the variance, respectively. They have been normalized as described below. They are statistically distinct from each other and the third EOF by North et al. (1982) criteria. The first EOF is associated with deep vertical motion (or subsidence) extending throughout the troposphere. The second EOF corresponds to upward (downward) vertical motion in the upper troposphere and subsidence (ascent) in the lower troposphere. The sign of the vertical motion in the second EOF switches around 650 hPa. The signs in the analysis have been chosen to have positive values corresponding to descent in the upper troposphere. The EOFs in Fig. 1a are invariant in space and time and were scaled/normalized to make

$$\frac{\int_{100\text{hPa}}^{1000\text{hPa}} \Omega_i(p)^2\, dp}{900\,\text{hPa}} = 1. \qquad (1)$$

This scaling choice affects the numerical values shown in Figs. 1b, 2, and 3, but not the patterns (e.g., a different scaling choice would multiply all numbers given by the same constant).

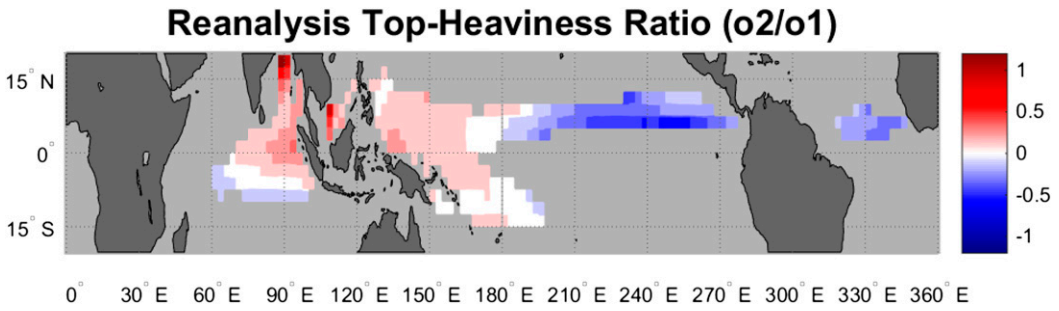

FIG. 2. Climatological top-heaviness ratio (mean amplitude of second principal component to mean amplitude of first principal component) as a function of location in reanalysis. This figure utilizes the analysis used to derive EOFS in Fig. 1. Colors correspond to vertical motion profile shapes shown in Fig. 1b.

Vertical motion can be approximated using the results of this principal component analysis. Following the notation of Back and Bretherton (2009b) we approximate the vertical motion:

$$\omega(x,y,p,t) = o_1(x,y,t)\Omega_1(p) + o_2(x,y,t)\Omega_2(p), \quad (2)$$

where $\Omega_1(p)$ and $\Omega_2(p)$ correspond to the EOFs shown in Fig. 1 and the associated principal components are denoted $o_1(x, y, t)$ and $o_2(x, y, t)$. The principal components $o_1(x, y, t)$ and $o_2(x, y, t)$ can alternatively be described as the amplitudes of the EOFs. This latter interpretation will be used to estimate them from satellite observations in the method described below. In this framework, under the assumption of two vertical modes, and once scaling choices are made for Ω_i, the shape of the vertical motion profile at a given location and time is a function of the ratio of $o_2(x, y, t)$ to $o_1(x, y, t)$ only. Figure 1b shows examples of vertical motion profiles constructed from the EOFs shown in Fig. 1a with a varying o_2/o_1 ratio. The vertical motion profiles shown are all normalized the same way as the basis functions were, as in Eq. (1). Varying o_1 and keeping the o_2/o_1 ratio the same keeps the shape of the vertical motion profile the same (e.g., upward velocity at one level relative to another is the same) but varies the magnitude of vertical motion at each level.

Figure 2 shows a global map of the ratio of reanalysis $o_2(x, y, t)/o_1(x, y, t)$, the amplitude of the second function (the second principal component o_2) to the amplitude

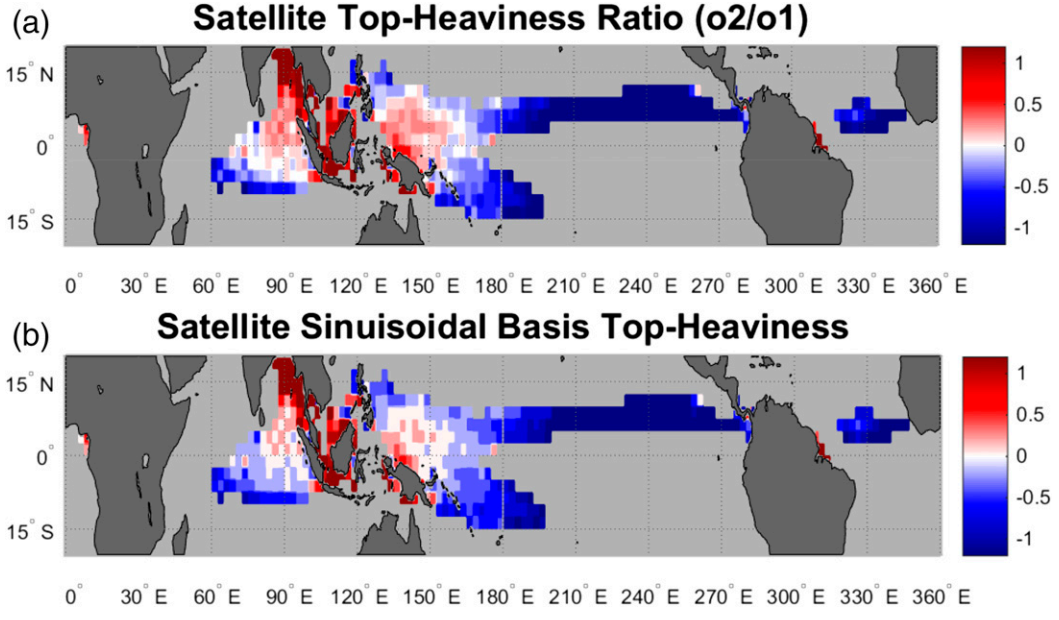

FIG. 3. (a) Top-heaviness ratio as in Fig. 2, estimated from satellite data, using the methodology of HB with basis functions shown in Fig. 1. (b) Utilizing sinusoidal basis functions and the same methodology shows that overall patterns are not sensitive to basis function choice. Color scale saturates at both ends.

of the first function [first principal component $o_1(x, y, t)$] in regions where the amplitude of time-mean o_1 corresponds to upward vertical motion [$o_1 < 0$ following sign conventions in Fig. 1a and Eq. (2)]. The ratio is shown in only regions with upward vertical motion because we are focusing on deep convective regions. The average of the numerator and denominator are calculated separately before the ratio is calculated to be consistent with Fig. 1b, so that the colors on this figure correspond to the ratios shown in Fig. 1b. The map can be thought of as a global map of top-heaviness. Blue regions correspond to more bottom-heavy circulations and red regions correspond to more top-heavy circulations. Note the strong contrast in the global map of vertical motion profile top-heaviness between the top-heavy vertical motion profiles of the western Pacific warm pool and the more bottom-heavy vertical motion profiles seen in the central and eastern Pacific and Atlantic intertropical convergence zones.

a. Satellite omega analysis

Substantial uncertainties exist in reanalysis vertical motion profiles, which are not directly constrained by observations. Thus, it is desirable to have a way to estimate vertical motion profile top-heaviness that does not depend directly on reanalysis. Luckily, the amplitudes of o_1 and o_2 can be estimated from satellite data using the methodology of Handlos and Back (2014, hereafter HB). In HB's method, the top-heaviness ratio can have some dependence on reanalysis-derived basis functions (Fig. 1a). However, HB also utilized idealized basis functions, as will this work, to mitigate this issue. The reanalysis EOFs likely give our best estimate of basis functions, while the idealized basis functions can be used to test the sensitivity of the results to basis function. In this work, we follow the methodology described in HB for estimating vertical motion profile shape using satellite data; spatial and temporal resolution of the data are described in HB, as are estimates of uncertainties. Satellite data comes from estimates of surface convergence (from QuikSCAT), precipitation (TRMM 3B42; TRMM 2016a), and radiative cooling (NASA's Energy and Water Cycle Study; Grecu and Olson 2006; Grecu et al. 2009; L'Ecuyer and Stephens 2003, 2007; L'Ecuyer and Mcgarragh 2010).

The concept behind the HB method utilizes the relationship between vertical motion, surface convergence, and precipitation. Assuming that vertical motion can be described by Eq. (2), and neglecting some small terms, the dry static energy budget can be used to relate vertical motion and precipitation via the following equation [Eq. (7) from HB]:

$$\mathrm{LP}(x,y,t) = M_{s1}o_1(x,y,t) + M_{s2}o_2(x,y,t) - \Delta F_{\mathrm{rad}}(x,y,t), \tag{3}$$

where ΔF_{rad} is the column-integrated radiative cooling, LP is the latent heating associated with precipitation, and gross dry stratifications M_{s1} and M_{s2} are denoted

$$M_{si} = \int_{p_0}^{p_t} \Omega_i \frac{\partial s}{\partial p}\frac{dp}{g}; \quad i = 1, 2. \tag{4}$$

In this equation, $s = C_pT + gz$ is the dry static energy, p_0 is 1000 hPa, p_t is 100 hPa and other terms have their conventional meteorological meanings. Gross dry stratifications are calculated from the mean s profile over the tropical oceans (in reanalysis), so these are assumed constant.

We wish to estimate o_2 and o_1 from satellite data, so another constraint is needed. For this we utilize surface convergence from QuikSCAT. This can be related to the amplitude of o_i via the following equation [HB; Eq. (10)]:

$$\nabla \cdot \mathbf{V}_{\mathrm{sfc}}(x,y,t) = c_1o_1(x,y,t) + c_2o_2(x,y,t), \tag{5}$$

where c_i are constants derived from Ω_i:

$$c_i = \frac{\Omega_i(975\,\mathrm{hPa}) - \Omega_i(1000\,\mathrm{hPa})}{25\,\mathrm{hPa}}. \tag{6}$$

These constants represent the amount of surface convergence per unit amplitude of vertical motion associated with the two basis functions.

The system of Eqs. (3) and (5), combined with the satellite data has two unknowns o_1 and o_2. Thus, we can solve for the shape of the vertical motion profile from the satellite data, either using the reanalysis-determined basis functions, or any other basis functions we choose. The basis functions are only used to calculate M_{si} and c_i.

Figure 3a shows the top-heaviness ratio (o_2/o_1) as estimated from satellite data using this methodology and the reanalysis-derived basis functions in regions where time-mean o_1 corresponds to upward vertical motion. Many of the broad-scale features are similar between Figs. 2 and 3a, but there are disagreements on smaller scales. As in Fig. 2, the eastern Pacific and Atlantic have more bottom-heavy vertical motion profiles, while the western Pacific and Indian Oceans have more top-heavy ratios. The most top-heavy region is in the Bay of Bengal in both cases. However, in the satellite data there is an asymmetry between the top-heaviness of the northern and southern part of the western Pacific ITCZ, with the northern part being more top-heavy. The details of which regions within the eastern Pacific and Atlantic are most bottom-heavy are also different. For example, in Fig. 2 there are notable north–south gradients in bottom-heaviness in the

TABLE 1. The correlation coefficients and RMS differences (in parentheses, where relevant) between quantities shown in Figs. 2–4 in regions where rainfall is greater than 5 mm day^{-1}.

	Reanalysis o_2/o_1	Satellite o_2/o_1	Idealized basis function satellite o_2/o_1
Reanalysis o_2/o_1	1.0	0.55 (0.013)	0.63 (0.014)
Satellite o_2/o_1	0.55 (0.013)	1.0	0.94 (0.004)
Idealized basis function satellite o_2/o_1	0.63 (0.014)	0.94 (0.004)	1.0
Stratiform rain fraction	−0.18	−0.13	−0.15
Shallow rain fraction	−0.36	−0.59	−0.57
Convective rain fraction	−0.04	−0.24	−0.21

eastern Pacific and Atlantic that are absent in Fig. 3a. The correlation between Figs. 2 and 3a is 0.55 (see Table 1), which shows that there is significant correlation, but also significant variability, between the two estimates of top-heaviness. With a very conservative (less conservative) assumption of 20 (100) degrees of freedom, 0.43 (0.19) would be a statistically significant correlation at the 95% level. Given the uncertainties in moist physics parameterization in the reanalysis and the difficulty simulating mean precipitation patterns in numerical models, the agreement between these methodologies on what regions are top-heavy is very noteworthy, despite being far from perfect.

Figure 3b shows the top-heaviness ratio estimated using idealized basis functions rather than reanalysis-derived basis functions. In this case, the first basis function is half a sine wave extending from 1000 to 100 hPa, and the second basis function is a full sine wave extending over the same depth. The fields shown in Figs. 3a and 3b are closely correlated with a correlation coefficient of 0.94, showing that the broad-scale patterns in Fig. 3a are not due to details of the reanalysis-derived basis functions. This supports the robustness of results and usefulness of our methodology for estimating top-heaviness. It shows that our best estimate of top-heaviness from satellite data, shown in this subsection, is not strongly influenced by reanalysis.

b. Rain type

Geographic variations in stratiform rain fraction (the fraction of the total rain falling in regions identified by radar as being stratiform) have been posited to be related to vertical motion top-heaviness (e.g., Schumacher et al. 2004; Houze 2004). Stratiform rain in this context is defined by how it appears on radar: fairly homogeneous in the horizontal with a layered structure on vertical cross sections. It often has a ''bright band'' or layer of high reflectivity in which ice particles are melting (Houze 1997). This is contrasted with convective precipitation, which has ''cells'' or horizontally localized patches or cores of intense radar reflectivity. In field campaigns, times with high stratiform rain fraction have been observed to correspond to times with more top-heavy vertical motion profiles (e.g., Houze 1989). However, it has also been noted that the heating profiles associated with convective rain are less consistent from case to case (Houze 1989).

Figure 4a shows stratiform rain fraction as seen by TRMM 3A25 in regions where precipitation is greater than 5 mm day^{-1}. The 5 mm day^{-1} threshold was chosen as a round number that covers a similar geographic area to the regions where upward vertical motion occurs (that this must be the case can be shown using variants on methods in HB). Stratiform rain in the TRMM 3A25 product is identified using a variant of the method developed by Steiner et al. (1995) according to the readme file (TRMM 2016b). The method judges whether a pixel is convective by comparing its reflectivity to that of an average intensity taken over a surrounding background. If the pixels intensity exceeds the surrounding background by a factor f, the pixel is considered to be convective. The threshold f depends on the background intensity, where the background intensity is the average reflectivity over some region. The functional form of f as a function of background intensity is calibrated to match a manual separation of convective and stratiform regions in regions where it is possible to identify a bright band. A bright band is considered a sufficient but not necessary condition for a region to be stratiform, as bright bands are not always seen in regions considered stratiform. Hence, the local intensity compared to background intensity is used to identify convective regions and the remaining regions are considered stratiform. Note that the vertical structure of the reflectivity is not directly used to estimate stratiform rain fraction, so the stratiform rain fraction metric does not directly provide information on vertical motion top-heaviness.

The stratiform rain fraction in Fig. 4a generally varies between 0.35 and 0.55 with most values in the center of that range. The region with highest stratiform rain fraction is in the eastern Pacific region where vertical motion profiles are bottom-heavy according to the metrics shown in Figs. 2 and 3. Higher values of stratiform rain fraction tend to also occur in the Atlantic, western Pacific, and

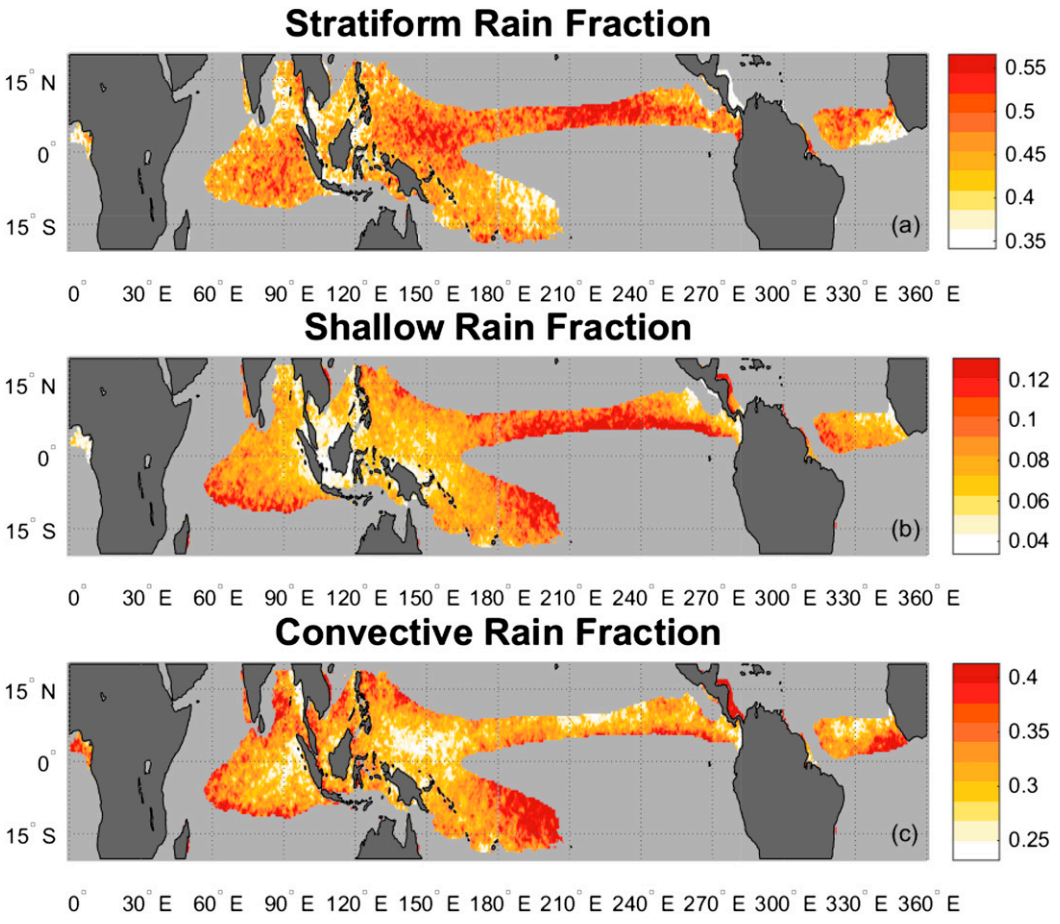

FIG. 4. (a) Climatological stratiform rain fraction, (b) shallow rain fraction, and (c) deep convective rain fraction in regions where precipitation is greater than 5 mm day^{-1} from TRMM 3A25 product. Color scale saturates at both ends.

some of the Indian Ocean. Lower values occur in the South Pacific convergence zone (SPCZ) the southeastern Atlantic ITCZ and north of 5°N, 45°–95°W. Note that there is no relationship between regions of high stratiform rain fraction and regions with top-heavy (or bottom-heavy) vertical motion profiles. Correlation coefficients between figures are shown in Table 1 for regions where data are shown in all previous figures. The part of the Pacific that has the most bottom-heavy vertical motion profiles, the central-eastern Pacific, has comparatively high stratiform rain fraction, above 0.5. This may seem surprising based on the arguments advanced in some earlier work (e.g., Schumacher et al. 2004; Houze 2004) that regions with more stratiform rain fraction are more top-heavy. Below, we discuss this finding and the relationship to existing studies further after examining shallow and convective rain fraction maps.

Climatological shallow rain fraction in regions with greater than 5 mm day^{-1} rainfall is shown in Fig. 4b. This quantity generally varies between 0.05 and 0.15 in deep convective regions. The regions with the largest shallow rain fractions are in the central to eastern Pacific ITCZ and on the eastern edge of the SPCZ. Lower shallow rain fractions occur in the western Pacific and around the Maritime Continent. They also occur in the eastern Pacific warm pool region. The larger shallow rain fraction in the central to eastern Pacific ITCZ is consistent with vertical motion in this region being more bottom-heavy and in general the shallow rain fraction appears to be higher where other metrics suggest more bottom-heavy vertical motion profiles. However, the overall shallow rain fraction, as well as its variations, is small enough that the dramatic vertical motion profile variations cannot be explained by this alone. Hence, the result that top-heaviness is not correlated with stratiform rain fraction cannot be explained by variations in shallow rain fraction alone.

Deep convective rain fraction (i.e., not including shallow rain) in these regions is shown in Fig. 4c. This quantity generally varies between 0.25 and 0.4. Comparatively low convective rain fraction occurs over the

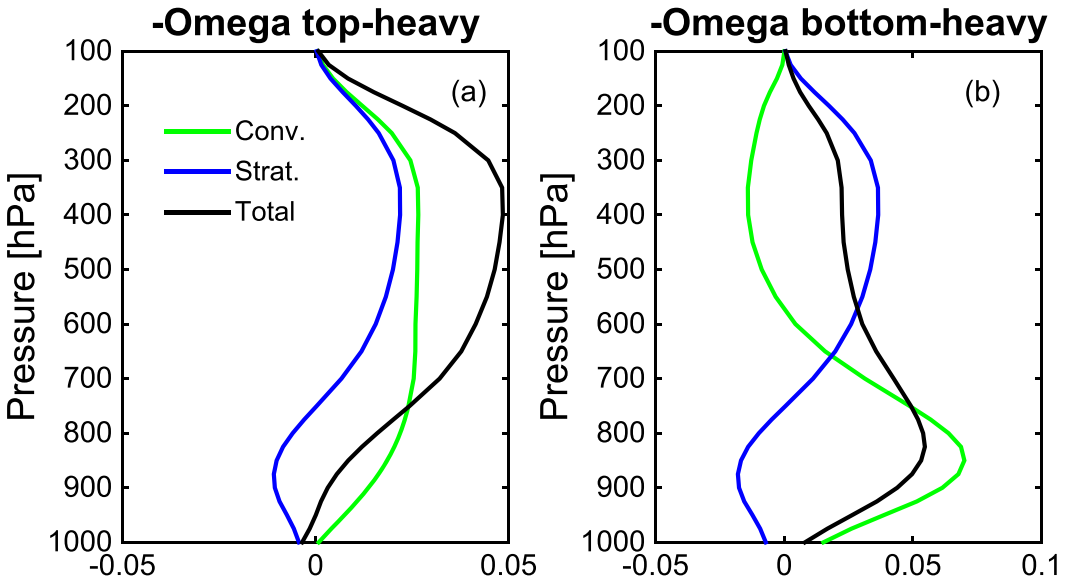

FIG. 5. An example of how geographically varying convective heating profiles can lead to stratiform rain fraction not being correlated with top-heaviness. (a) Hypothetical example for top-heavy region of the contribution of convective and stratiform vertical motion to the total profile, as well as total profile (sum of the convective, stratiform profiles). (b) Hypothetical example for a bottom-heavy region. Stratiform rain fraction is higher in (b) (0.55) than in (a) (0.35). See text for details.

north-central to northeastern Pacific ITCZ (210°–240°E), in the western Pacific (130°–160°E), and over the northern part of the Atlantic Ocean. As seen in previous figures, these regions have quite varied vertical motion profiles ranging from quite bottom-heavy to quite top-heavy. This may be because the shape of the convective latent heating profile varies geographically owing to geographic variations in the depth of the convection in these regions. Back and Bretherton (2009a,b) elucidated reasons for variations in the depth of convection. Geographic variations in convective heating profiles are consistent with the fact that ground-based observations have shown that vertical motions in convective regions are variable, as noted in Houze (1989).

3. Why stratiform rain fraction may not explain top-heaviness

Returning to the seemingly surprising result that stratiform rain fraction is not correlated with top-heaviness, we now discuss how this can be reconciled with existing literature on this subject. Ground-based observations are generally considered more reliable than satellite data, and these show stratiform profiles are more top-heavy (e.g., Houze 1989) than convective heating profiles. Our results are not contradicting that finding. In fact, we examined the top-heaviness ratio used here as a function of stratiform rain fraction in the region where the Tropical Ocean and Global Atmosphere Coupled Ocean–Atmosphere Response Experiment (TOGA COARE; Webster and Lukas 1992) took place and found that top-heaviness (satellite derived and reanalysis) in that region increases monotonically when binned by stratiform rain fraction (not shown). However, if there is any significant variability within convective heating profiles, as there may be from region to region, the well-known finding does not necessarily imply that a larger stratiform rain fraction must be associated with more top-heavy vertical motion profiles. Mathematically, this insight comes from the fact that stratiform and convective heating profiles do not need to be orthogonal as described below.

An illustrative counterexample to the common view [as in Schumacher et al. (2004)] that regions with higher stratiform rain fraction are more top-heavy is shown in Fig. 5. Figure 5a shows the contributions to vertical motion of a hypothetical top-heavy convective heating profile, and a hypothetical stratiform profile, as well as the sum of the two, for a case with stratiform rain fraction 0.3. Figure 5b shows contributions to vertical motion of a hypothetical bottom-heavy heating profile, with stratiform rain fraction 0.5. We describe how this figure was constructed below. It illustrates that it is possible for higher stratiform rain fraction to be associated with a more bottom-heavy vertical motion profile if convective heating profiles vary enough.

To construct each subpanel in this figure, we use a linear system of four equations. The unknowns in the

equation are amplitudes of convective and stratiform Ω_i. We denote the convective vertical motion profiles

$$\omega_c(p,x) = o_{1,c}(x)\Omega_1(p) + o_{2,c}(x)\Omega_2(p) \tag{7}$$

and stratiform vertical motion

$$\omega_s(p,x) = o_{1,s}(x)\Omega_1(p) + o_{2,s}(x)\Omega_2(p). \tag{8}$$

We assume total rainfall (due to convective plus stratiform vertical motion) in both cases is $10\,\mathrm{mm\,day^{-1}}$ and radiative cooling corresponds to $5\,\mathrm{mm\,day^{-1}}$ of precipitation (these are reasonable values for the ITCZ). Working from Eq. (3), this gives us an equation for overall rainfall (the same equation for both panels):

$$\begin{aligned} L'(10\,\mathrm{mm\,day^{-1}}) = {} & M_{s1}(o_{1,c} + o_{1,s}) \\ & + M_{s2}(o_{2,c} + o_{2,s}) \\ & - L'(5\,\mathrm{mm\,day^{-1}}), \end{aligned} \tag{9}$$

where L' is the latent heat of condensation divided by the number of seconds in a day. In the top-heavy panel, the total vertical motion top-heaviness ratio is 0.4, while this measure is -0.4 in the bottom-heavy panel. This gives us a second equation for both cases. For the top-heavy case, this is

$$\frac{o_{2,c} + o_{2,s}}{o_{1,c} + o_{1,s}} = 0.4. \tag{10}$$

For the bottom-heavy case -0.4 is substituted for 0.4. In both cases, the top-heaviness ratio of the vertical motion associated with stratiform rain is assumed to be the same: 1.1. This gives us a third equation:

$$\frac{o_{2,s}}{o_{1,s}} = 1.1. \tag{11}$$

The fourth equation comes from the stratiform rain fraction. For this equation, we need to make an assumption about how much of the precipitation associated with radiative cooling is stratiform precipitation. We assume this fraction is the same as the overall stratiform rain fraction, but the nature of the figures is not particularly sensitive to this assumption. For the top-heavy case with stratiform rain fraction 0.3, this yields the following equation for stratiform rainfall:

$$\begin{aligned} L'(0.3 \times 10\,\mathrm{mm\,day^{-1}}) = {} & M_{s1}o_{1,s} + M_{s2}o_{2,s} \\ & - L'(0.3 \times 5\,\mathrm{mm\,day^{-1}}). \end{aligned} \tag{12}$$

For the bottom-heavy case, 0.5 is substituted in for 0.3 as the stratiform rain fraction. We solve the corresponding linear system of equations to find the convective and stratiform profiles shown.

Figure 5b has more stratiform vertical motion (67% more) and the stratiform profiles are always much more top-heavy than convective heating profiles in this example. However, the variations in the shape of the convective heating profiles between Figs. 5a and 5b are more than large enough to make up for the variations in stratiform heating amount and, hence, the overall heating profile is significantly more top-heavy in the first case. This example demonstrates that stratiform heating profiles can be more top-heavy than convective heating profiles everywhere, without this implying that a higher stratiform rain fraction must be associated with more top-heavy profiles.

Another possible factor contributing to the lack of correlation between stratiform rain fraction and top-heaviness is that the heating profiles associated with what is identified as stratiform regions are varying geographically. Houze et al. (2015) described scenes identified by the TRMM 2A23 algorithm as stratiform that consist of "closely spaced, weak and shallow vertically oriented echoes or cells" and have a "faint, but nearly continuous bright band [that] extends horizontally across the region of weak cells" (see their Figs. 12b,d,f,h). They noted that it is doubtful that these types of stratiform regions have heating profiles like those associated with the stratiform regions of mesoscale convective systems (MCS) and posited that the cellular stratiform echoes in ITCZ regions may be associated with a shallow overturning mode. Also, Houze (1989) showed some variations in the height of maximum heating and relative amplitude between top heating and bottom heating/cooling in stratiform precipitation regions (see their Figs. 16–18). Hence variations in stratiform heating profiles could contribute to the finding that stratiform rain fraction is not correlated with top-heaviness.

Stratiform rain fraction is measured only when it is raining, while vertical motion top-heaviness integrates over both raining and nonraining times. This might be argued to be an additional issue with the idea that stratiform rain fraction explains vertical motion profiles. However, as Eq. (3) makes clear, there is a direct relationship between the amount of vertical motion and the rainfall, provided radiative cooling varies little. Hence, vertical motion is also to first order effectively "weighted" by rainfall; for example, the vertical motion profiles that contribute more to rainfall also contribute more to overall vertical motion. Thus, it makes sense from that perspective to compare stratiform rain fraction and top-heaviness ratio as we have done, rather than utilizing a precipitation-weighted top-heaviness ratio.

Overall, our results clearly warn that one should not always assume that higher stratiform rain fractions are associated with more top-heavy vertical motion profiles (even if shallow heating is comparable).

4. Conclusions

We introduced a new methodology for visualizing geographic variability in the climatological top-heaviness of vertical motion profiles in deeply convecting regions using reanalysis data. This reanalysis top-heaviness was compared to that estimated using the satellite-based methodology of HB. The reanalysis and satellite-based methodologies agree on which regions are more top-heavy or bottom-heavy, but the satellite-based methodology tends to produce larger variations from bottom-heavy to top-heavy vertical motion profiles. Notably, climatological stratiform rain fraction as measured by TRMM was not correlated with top-heaviness or bottom-heaviness, at odds with what some past studies have posited. Shallow rain fraction variations were not large enough to explain the major variations in top-heaviness. The lack of relationship between stratiform rain fraction and top-heaviness is likely due to 1) geographic variations in the depth of convective heating profiles and/or 2) variations in stratiform heating profiles, potentially associated with ''cellular'' type stratiform heating profiles substantially different than MCS stratiform heating.

A notable result in this study and other findings (e.g., Back and Bretherton 2006) is that the eastern Pacific ITCZ has bottom-heavy vertical motion profiles but high stratiform rain fraction values (e.g., Schumacher et al. 2004). This suggests that deep convection is behaving differently in this region than has been documented in previous field campaigns. Back and Bretherton (2009b) argued that the bottom-heavy vertical motion profiles exist as a result of strong SST gradients in this region and relatively low SST. This may lead to either very bottom-heavy convective heating profiles (as in Fig. 5b) and/or stratiform heating associated with weak convection that does not go very deep. Finding out which of these possibilities (or others) is going on is worthy of further study. As described in the introduction, this has implications for retrieval and understanding of latent heating and vertical profiles from satellite data. This suggests that a field campaign in the eastern Pacific ITCZ that could shed light on this issue would have broad utility.

Acknowledgments. This research was supported by NASA Grant NNX12AL96G and NSF Grant MSN188169. Thanks to Kuniaki Inoue for coming up with the idea to produce Fig. 1b. The comments of Matthew Igel and two anonymous reviewers have improved the manuscript.

REFERENCES

Adam, O., T. Bischoff, and T. Schneider, 2016: Seasonal and interannual variations in the energy flux equator and ITCZ. Part II: Zonally varying shifts in the ITCZ. *J. Climate*, **29**, 7281–7293, doi:10.1175/JCLI-D-15-0710.1.

Back, L. E., and C. S. Bretherton, 2006: Geographic variability in the export of moist static energy and vertical motion profiles in the tropical Pacific. *Geophys. Res. Lett.*, **33**, L17810, doi:10.1029/2006GL026672.

——, and ——, 2009a: On the relationship between SST gradients, boundary layer winds, and convergence over the tropical oceans. *J. Climate*, **22**, 4182–4196, doi:10.1175/2009JCLI2392.1.

——, and ——, 2009b: A simple model of climatological rainfall and vertical motion patterns over the tropical oceans. *J. Climate*, **22**, 6477–6497, doi:10.1175/2009JCLI2393.1.

Bretherton, C. S., and P. K. Smolarkiewicz, 1989: Gravity waves, compensating subsidence and detrainment around cumulus clouds. *J. Atmos. Sci.*, **46**, 740–759, doi:10.1175/1520-0469(1989)046<0740:GWCSAD>2.0.CO;2.

Charney, J. G., 1963: A note on large-scale motions in the tropics. *J. Atmos. Sci.*, **20**, 607–609, doi:10.1175/1520-0469(1963)020<0607:ANOLSM>2.0.CO;2.

Dee, D. P., and Coauthors, 2011: The ERA-Interim reanalysis: Configuration and performance of the data assimilation system. *Quart. J. Roy. Meteor. Soc.*, **137**, 553–597, doi:10.1002/qj.828.

Frierson, D. M., and Coauthors, 2013: Contribution of ocean overturning circulation to tropical rainfall peak in the Northern Hemisphere. *Nat. Geosci.*, **6**, 940–944, doi:10.1038/ngeo1987.

Grecu, M., and W. S. Olson, 2006: Bayesian estimation of precipitation from satellite passive microwave observations using combined radar–radiometer retrievals. *J. Appl. Meteor. Climatol.*, **45**, 416–433, doi:10.1175/JAM2360.1.

——, ——, C. L. Shie, T. S. L'Ecuyer, and W. K. Tao, 2009: Combining satellite microwave radiometer and radar observations to estimate atmospheric heating profiles. *J. Climate*, **22**, 6356–6376, doi:10.1175/2009JCLI3020.1.

Handlos, Z. J., and L. E. Back, 2014: Estimating vertical motion profile shape within tropical weather states over the oceans. *J. Climate*, **27**, 7667–7686, doi:10.1175/JCLI-D-13-00602.1.

Hartmann, D., H. Hendon, and J. R. A. Houze, 1984: Some implications of the mesoscale circulations in cloud clusters for large-scale dynamics and climate. *J. Atmos. Sci.*, **41**, 113–121, doi:10.1175/1520-0469(1984)041<0113:SIOTMC>2.0.CO;2.

Houze, R. A., Jr., 1989: Observed structure of mesoscale convective systems and implications for large-scale heating. *Quart. J. Roy. Meteor. Soc.*, **115**, 425–461, doi:10.1002/qj.49711548702.

——, 1997: Stratiform precipitation in regions of convection: A meteorological paradox? *Bull. Amer. Meteor. Soc.*, **78**, 2179–2196, doi:10.1175/1520-0477(1997)078<2179:SPIROC>2.0.CO;2.

——, 2004: Mesoscale convective systems. *Rev. Geophys.*, **42**, RG4003, doi:10.1029/2004RG000150.

——, K. L. Rasmussen, M. D. Zuluaga, and S. R. Brodzik, 2015: The variable nature of convection in the tropics and subtropics: A legacy of 16 years of the Tropical Rainfall Measuring Mission satellite. *Rev. Geophys.*, **53**, 994–1021, doi:10.1002/2015RG000488.

Kang, S. M., D. M. W. Frierson, and I. M. Held, 2009: The tropical response to extratropical thermal forcing in an idealized GCM: The importance of radiative feedbacks and convective parameterization. *J. Atmos. Sci.*, **66**, 2812–2827, doi:10.1175/2009JAS2924.1.

L'Ecuyer, T. S., and G. L. Stephens, 2003: The tropical oceanic energy budget from the TRMM perspective. Part I: Algorithm and uncertainties. *J. Climate*, **16**, 1967–1985, doi:10.1175/1520-0442(2003)016<1967:TTOEBF>2.0.CO;2.

——, and ——, 2007: The tropical atmospheric energy budget from the TRMM perspective. Part II: Evaluating GCM representations of the sensitivity of regional energy and water cycles to the 1998–99 ENSO cycle. *J. Climate*, **20**, 4548–4571, doi:10.1175/JCLI4207.1.

——, and G. Mcgarragh, 2010: A 10-year climatology of tropical radiative heating and its vertical structure from TRMM observations. *J. Climate*, **23**, 519–541, doi:10.1175/2009JCLI3018.1.

North, G. R., T. L. Bell, and R. F. Cahalan, 1982: Sampling errors in the estimation of empirical orthogonal functions. *Mon. Wea. Rev.*, **110**, 699–706, doi:10.1175/1520-0493(1982)110<0699:SEITEO>2.0.CO;2.

Schneider, T., T. Bischoff, and G. H. Haug, 2014: Migrations and dynamics of the intertropical convergence zone. *Nature*, **513**, 45–53, doi:10.1038/nature13636.

Schumacher, C., R. A. Houze, and I. Kraucunas, 2004: The tropical dynamical response to latent heating estimates derived from the TRMM precipitation radar. *J. Atmos. Sci.*, **61**, 1341–1358, doi:10.1175/1520-0469(2004)061<1341:TTDRTL>2.0.CO;2.

Sherwood, S. C., S. Bony, and J.-L. L. Dufresne, 2014: Spread in model climate sensitivity traced to atmospheric convective mixing. *Nature*, **505**, 37–42, doi:10.1038/nature12829.

Sobel, A. H., and C. S. Bretherton, 2000: Modeling tropical precipitation in a single column. *J. Climate*, **13**, 4378–4392, doi:10.1175/1520-0442(2000)013<4378:MTPIAS>2.0.CO;2.

Steiner, M., R. A. Houze Jr., and S. E. Yuter, 1995: Climatological characterization of three-dimensional storm structure from operational radar and rain gauge data. *J. Appl. Meteor.*, **34**, 1978–2007, doi:10.1175/1520-0450(1995)034<1978:CCOTDS>2.0.CO;2.

TRMM, 2016a: Readme for TRMM product 3B42 (v7). Goddard Earth Sciences Data and Information Services Center, accessed January 2016. [Available online at http://disc.sci.gsfc.nasa.gov/precipitation/documentation/TRMM_README/TRMM_3B42_readme.shtml.]

——, 2016b: TRMM product level 2A precipitation radar (PR) rain characteristics (2A23). Goddard Earth Sciences Data and Information Services Center, accessed January 2016. [Available online at https://disc.gsfc.nasa.gov/precipitation/documentation/TRMM_README/TRMM_2A23_readme.shtml.]

Webster, P. J., and R. Lukas, 1992: TOGA COARE: The coupled ocean–atmosphere response experiment. *Bull. Amer. Meteor. Soc.*, **73**, 1377–1416, doi:10.1175/1520-0477(1992)073<1377:TCTCOR>2.0.CO;2.

Wu, Z., E. S. Sarachik, and D. S. Battisti, 2000: Vertical structure of convective heating and the three-dimensional structure of the forced circulation on an equatorial beta plane. *J. Atmos. Sci.*, **57**, 2169–2187, doi:10.1175/1520-0469(2000)057<2169:VSOCHA>2.0.CO;2.

Yanai, M., S. Esbensen, and J.-H. Chu, 1973: Determination of bulk properties of tropical cloud clusters from large-scale heat and moisture budgets. *J. Atmos. Sci.*, **30**, 611–627, doi:10.1175/1520-0469(1973)030<0611:DOBPOT>2.0.CO;2.